Thermal conductivity of micromachined low-stress silicon-nitride beams from 77 to 325 K

Rubina Sultan,[a] A. D. Avery, G. Stiehl, and B. L. Zink[b]
Department of Physics and Astronomy, University of Denver, Denver, Colorado 80208, USA

(Received 14 July 2008; accepted 4 January 2009; published online 17 February 2009)

We present thermal conductivity measurements of micromachined 500 nm thick silicon-nitride (Si–N) beams suspended between two Si–N islands, in the temperature range from 77 to 325 K. The measured thermal conductivity, k, of Si–N at high temperatures is in good agreement with previously measured values for Si–N grown by low-pressure chemical vapor deposition, but behaves much differently as temperature is lowered, showing a dependence more similar to polycrystalline materials. Preliminary structural characterization by x-ray diffraction suggests that the material is likely nano- or polycrystalline. The micromachined suspended platform structure is designed to allow highly accurate measurements of the thermal conductivity of deposited metallic, semiconducting, or insulating thin films. As a demonstration, we present measurements of a 200 nm thick sputtered molybdenum film. In the entire temperature range the measured thermal conductivity matches the prediction of the Wiedemann–Franz thermal conductivity determined from measured electrical conductivity. © *2009 American Institute of Physics*. [DOI: 10.1063/1.3078025]

I. INTRODUCTION

Thermal conductivity, k, is an important fundamental property that is often difficult to measure for materials in thin film form. In recent years, micro- or nanofabrication techniques have allowed advances in both technical achievement and fundamental science. Many of the resulting devices are built using thin films, where thermal properties can often differ from bulk materials. For metals at high temperatures, k is often estimated using the Wiedemann–Franz Law, which relates the electronic thermal conductivity to electrical conductivity for bulk metals where electrons dominate k. This law describes only the electronic transport and is valid over a wide range of temperatures for bulk samples. However, insulating or nanoscaled samples require measurements of thermal conductivity.[1–3] There are several well-established techniques for measuring the thermal properties of thin films in certain regimes, including the 3-ω method[4] and picosecond thermoreflectance.[5,6] These predominantly measure the thermal conductivity in the direction perpendicular to the film's supporting substrate (often called the cross-plane thermal conductivity). As shown in Fig. 1, we have designed a micromachined platform for thermal conductivity measurements using suspended Si–N membranes which provide a strong, low-stress, electrically insulating substrate that is a fairly poor conductor of heat. Accurate knowledge of the thermal conductivity of this Si–N is important because it is the single contribution to the background thermal conductance of our device. Similar Si–N structures are also commonly used to thermally isolate sensitive thermal detectors, both bolometers and microcalorimeters, operated at low temperatures.[7] The thermal transport in these Si–N films is often critical to optimal design of these devices. There is also fundamental interest in the thermal conductivity of this highly disordered material with strong covalent bonds.[8–10]

In this paper we describe an experimental technique for measuring the in-plane thermal conductivity of a wide range of thin films and we present the measured thermal conductivity of ~500 nm thick, low-stress, Si–N beams in the temperature range 77–325 K. By carefully controlling the geometry of the structure, we have dramatically reduced the radiation contribution to effective thermal conductance, which often complicates steady state measurements of thermal conductivity at temperatures above 100 K. We also present the measurement of thermal conductivity of a metal by direct deposition of a 200 nm thick molybdenum sample thin film on the Si–N beam and compare the results to the prediction of the Wiedemann–Franz law.

II. DEVICE FABRICATION

The fabrication process starts with a 3 in. (100) oriented Si wafer with a 500 nm thick layer of silicon-nitride coated on both sides by low-pressure chemical vapor deposition (LPCVD). This film is grown at 835 °C, from 12 SCCM (SCCM denotes cubic centimeter per minute at STP) of ammonia (NH_3) and 59 SCCM of dichlorosilane, at a process pressure of 250 mTorr. The resulting low-stress film is silicon rich compared to the stoichiometric composition (Si_3N_4). After the Si–N deposition, a 200 nm metal (Mo) layer is sputtered on the polished front side of the wafer and patterned into heaters and thermometers using standard optical lithography. Windows are etched in the Si–N layer via plasma etching (CF_4). Finally, the Si substrate beneath the patterned Si–N is removed using a KOH wet etch at 70 °C for 5 hours. This releases the Si–N structure leaving freely suspended islands (see Fig. 1). Since the KOH etch stops only when a (111) plane of silicon meets the Si–N layer, the orientation of the islands, legs, and beam at 45° angles to the

[a]Electronic mail: rsultan@du.edu.
[b]Electronic mail: barry.zink@du.edu.

 © 2009 American Institute of Physics

Author complimentary copy. Redistribution subject to AIP license or copyright, see http://jap.aip.org/jap/copyright.jsp

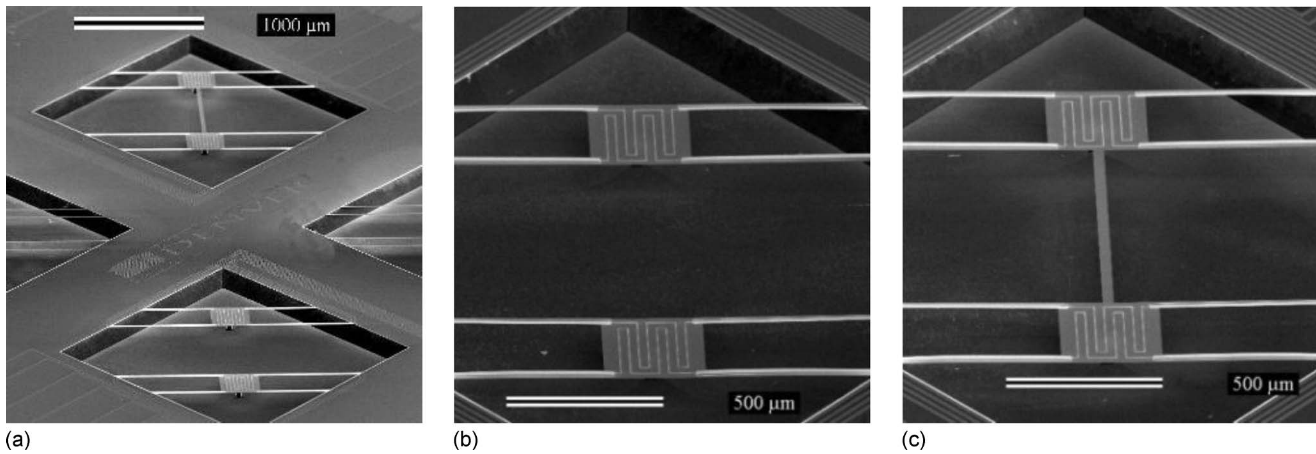

FIG. 1. Left: Overall view of device A and device B fabricated on a single 1×1 cm^2 Si chip, Middle: device A with two 250×250 μm^2 islands connected to the Si frame through eight legs with Mo heaters and thermometers patterned on each. Right: device B with two Si–N islands connected together by a 806 μm long, 35 μm wide, and 500 nm thick Si–N suspended beam.

(100) direction allows these structures to be completely undercut by the anisotropic KOH etch. Figure 1(a) shows the scanning electron microscopy (SEM) images of two micromachined devices fabricated on a 1×1 cm^2 Si chip, taken after tilting the sample stage. In each device, two Si–N islands are suspended over a 2×2 mm^2 etch pit via Si–N legs. In device A there is no link between the islands, while in device B a Si–N beam bridges them. Figures 1(b) and 1(c) are magnified views of the two devices.

III. MEASUREMENT TECHNIQUE

Steady state measurements of thermal conductivity in this temperature range are often complicated by radiation losses. For example, in measurements of thin film thermal conductivity made with a micromachined membrane calorimeter,[11] radiation contributes significantly to effective thermal conductance above 100 K. This was one of the main motivations for the development of the 3-ω method,[4] which uses an ac technique to eliminate radiation effects. Although this technique is popular, it is useful only above $\sim$30 K, and almost exclusively measures in the direction perpendicular to the substrate. One goal of our design is to minimize radiation effects by significantly reducing the heated area of the device.

Figure 2 shows the thermal models of three different devices. Figure 2(a) is the thermal model of device A, where thermal conductance (K_L) occurs only through the legs when power (P_h) is applied to the heater on one of the islands. Figure 2(b) shows a thermal model of device B where a thermal conductance path (K_B) is added through the Si–N beam connecting the two islands. Figure 2(c) shows the thermal model of device C where (K_S) shows the deposited sample thin film on the Si–N beam which increases the thermal conductance through the beam as compared to device B. The power dissipated in a device of type A as a function of temperature, T_0, is potentially affected by both conduction and radiation so that

$$P=\langle K_L(T_h,T_0)\rangle\Delta T+A_{\text{eff}}\epsilon_{\text{eff}}\sigma[(T_0+\Delta T)^4-T_0^4], \qquad (1)$$

where the first term represents the thermal conduction and is the average value of K_L between T_0 and T_h, $\Delta T=T_h-T_0$, and the second term describes radiation emitted by the heated area of the device and absorbed from the environment. Here A_{eff} and ϵ_{eff}, respectively, are the effective area and emissivity of the heated area of the device, and σ is the Stefan–Boltzmann radiation constant. Taylor expansion of the first term and simplification after keeping terms up to ΔT^2 gives

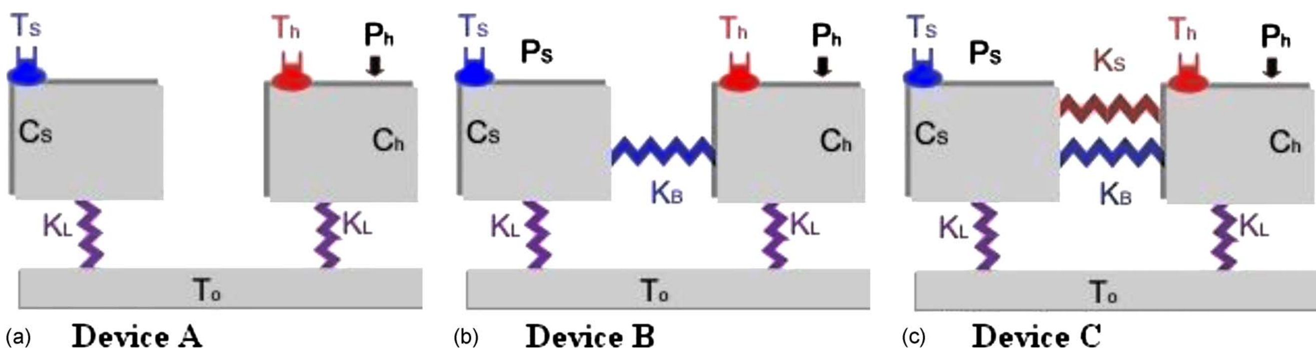

FIG. 2. (Color online) (a) Thermal model of device A with no Si–N beam between islands, (b) thermal model of device B with Si–N beam bridging two islands and (c) thermal model of device C with sample thin film deposited on Si–N beam.

Author complimentary copy. Redistribution subject to AIP license or copyright, see http://jap.aip.org/jap/copyright.jsp

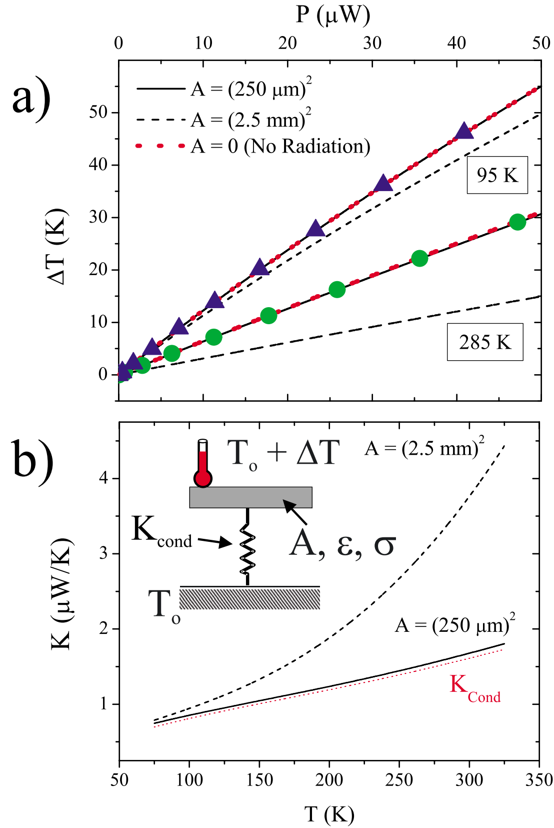

FIG. 3. (Color online) (a) Predicted ΔT vs P for a simple model of the thermal platform that includes radiation losses at two temperatures, 95 K (upper lines) and 285 K (lower lines). The solid lines are calculated for a platform with a (250 μm)^2 heated area, dashed lines for a (2.5 mm)^2 heated area, and dotted line for no radiation contribution. The symbols represent measured values for device A, which match the low radiation loss prediction extremely well. (b) Predicted $K=\Delta T/P$ for the radiation models. The upturn caused by radiation losses would complicate thermal transport measurements for large-area platforms. Inset: Schematic of the simple thermal radiation model.

$$P = (K_L(T_0) + 4A_{\mathrm{eff}}\epsilon_{\mathrm{eff}}\sigma T_0^3)\Delta T + \left(\frac{1}{2}\left.\frac{dK_L}{dT}\right|_{T_0} + 6A_{\mathrm{eff}}\epsilon_{\mathrm{eff}}\sigma T_0^2\right)\Delta T^2. \quad (2)$$

Therefore, if radiation losses are significant, a plot of ΔT versus P will have a reduced slope and show somewhat increased curvature. An example using a simple model of a heated platform connected to a thermal bath via a single thermal link is shown in Fig. 3. In this model we consider thermal platforms with two different effective areas, but with the same emissivity (here chosen to be $\epsilon=0.05$ as previously reported for similar micromachined devices[11]), and the same thermal link to the bath. In order to directly compare the predictions of Eq. (2) to our data, we used measured values of the thermal link, K_L, and its first derivative for device A, which will be discussed further below. Figure 3(a) shows the predicted ΔT for a range of heater powers, determined from the positive root of Eq. (2) for two different temperatures. In addition to the two different areas, the curve with no radiation terms is shown. The model device with $A=(2.5\ \text{mm})^2$ leads to larger radiation losses, while the 100 times smaller area of our thermal platform leads to no appreciable radiation loss. Figure 3(b) shows $K=P/\Delta T$ versus T_0 that would result from the model calculations. As seen previously in membrane nanocalorimeters with large heated areas,[11,12] the radiation loss causes a pronounced upturn above 100 K. Use of such microcalorimeters for thermal conductivity measurements relies on correction for these radiation losses, which adds considerably to measurement errors.[11] The simple reduction in the size of the heated platform leads to only very small deviations from the zero-radiation limit.

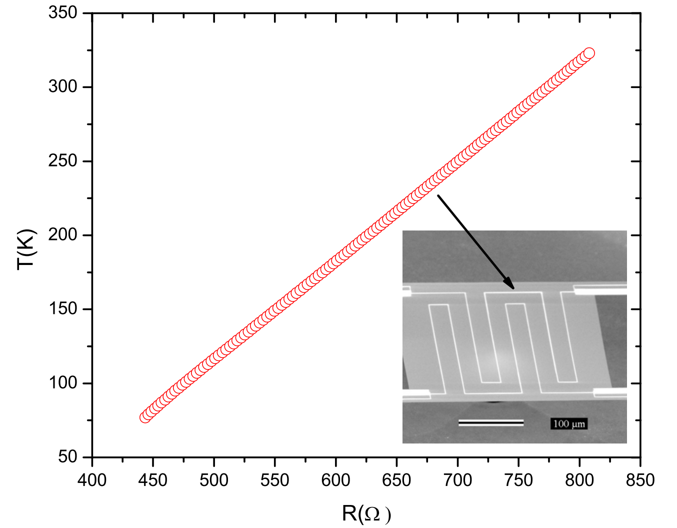

FIG. 4. (Color online) Example calibration of the micromachined thermometer. Inset: SEM micrograph of Mo wires patterned as thermometer and heater (the four wires used to measure each resistor are also visible).

To directly test for radiation effects, we perform a series of measurements on device A which has two Si–N suspended islands but no Si–N beam. Each island in this device is therefore a good approximation of the simple model used to estimate radiation losses above. As for the remaining measurements, we mount the device to the cold stage of a sample-in-vacuum cryostat on a Au plated copper sample holder, and ultrasonically wire bond the device heaters and thermometers to a circuit board that provides connections to room temperature. The board and the device are covered with a radiation shield to provide an isothermal environment. Vacuum of 3.0×10^{-6} Torr or better is maintained in the cryostat to prevent heat conduction through environmental gases around the sample holder and device.

Measurements with the thermal platform begin by regulating the temperature of the sample stage (and device frame) at T_{ref}. The maximum drift allowed for the reference temperature is 4 mK/min. To calibrate the platform, we then measure the resistance of each thermometer using a four-wire technique and a commercially available ac bridge while the sample stage temperature is controlled at T_{ref}. The maximum power dissipated in the thermometer while making these measurements is much lower than a nanowatt. The deviation of temperature on the device frame thermometer (T_0) is very small (≈ 3 mK) throughout the temperature range.

Figure 4 shows the calibration curve for the frame thermometer of device A. After this calibration step one of the islands is heated by applying a known current to the heater wire on the island. After heating, the temperatures on the

Author complimentary copy. Redistribution subject to AIP license or copyright, see http://jap.aip.org/jap/copyright.jsp

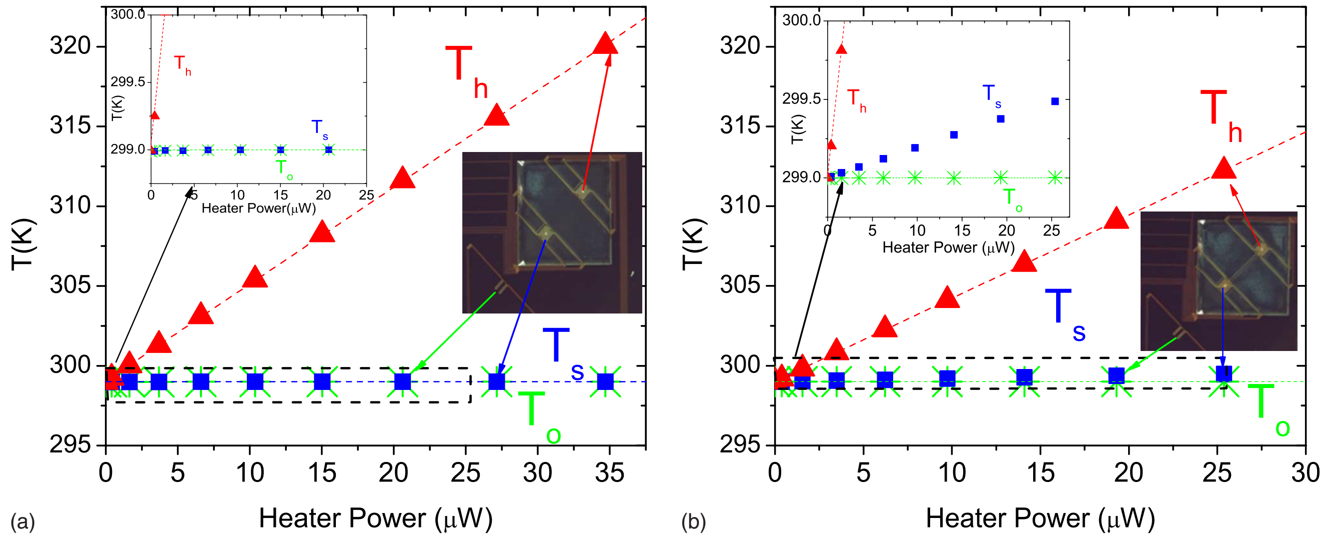

FIG. 5. (Color online) Temperature vs heater power at T_{ref}=299 K for (a) device A and (b) device B. T_0 (x's), T_h (triangles), and T_s (boxes) are the temperatures on frame, hot island, and cold island, respectively. Lower right insets: optical image of devices. Upper left insets: zoomed in regions for low heater power.

frame, hot island, and cold island are measured by again measuring the resistances. We also monitor the voltage drop on the heater to directly measure the applied power. We repeat this procedure for a series of heater currents, such that heater power is in the range 0.2–17.5 μW while the power dissipated in each of the thermometers remains less than 1 nW. The standard deviation of the frame temperature, T_0, for all applied powers at sample stage temperatures, T_{ref}=77, 149, and 299 K are ±2.72, ±3.90, and ±1.68 mK, respectively. This very small standard deviation shows that the temperature of the device frame remains exceptionally stable during our measurements.

Figure 5(a) shows a plot of the temperature on each of the islands versus power applied to the heater on one of the islands, at a constant reference temperature of 299 K for device A. As the heater power increases, the temperature on the hot island also increases as expected. However, the temperature of both the cold island and on the frame remains constant at the reference temperature (T_{ref}). We also verified that $\Delta T = T_{hot} - T_0$ as a function of power applied matches the prediction of the radiation model as shown in Fig. 3(a). Both of these facts indicate that in this structure we have reduced the radiation contribution significantly. Since in device A the legs form the only thermal link from the hot island to the thermal bath, thermal conductance through the legs is then calculated using

$$K = \frac{P}{\Delta T}, \tag{3}$$

where P is the measured power and ΔT is the average temperature gradient across each leg of the hot island.

A. Thermal conductivity of Si–N beam

When a Si–N beam bridges the two islands, the thermal conductance is not only through the legs but also through the Si–N beam, leading to the thermal model shown in Fig. 2(b), which is similar to that used to analyze measurements of thermal transport in nanostructures.[2] Figure 5(b) shows a plot of temperatures on both islands and on the frame versus power at a reference temperature of 299 K for the Si–N beam microstructure (device B). In this case as the power applied increases on the hot island, the temperature on the cold island also increases by a small but clearly measurable amount as heat flows from the island along the beam. The temperature on the frame (T_0) remains constant at T_{ref}. The rate of heat flow in the structure can be written mathematically as

$$C_h \frac{\partial T_h}{\partial t} = - K_L(T_h - T_0) - K_B(T_h - T_s) + P_h, \tag{4}$$

$$C_s \frac{\partial T_h}{\partial t} = - K_L(T_s - T_0) - K_B(T_s - T_h) + P_s, \tag{5}$$

where T_0, T_s, and T_h are the temperatures on frame, cold island, and hot island, respectively. C_h, C_s, P_h, and P_s are the specific heats and power dissipated on hot and cold islands, respectively. K_L and K_B are the thermal conductance through the legs and through the beam. In a steady state measurement, the time dependent term vanishes and since we do not apply power to the cold island, we set P_s=0, which gives

$$0 = - K_L(T_h - T_0) - K_B(T_h - T_s) + P_h, \tag{6}$$

$$0 = - K_L(T_s - T_0) - K_B(T_s - T_h). \tag{7}$$

Solving these equation for T_h and T_s with P_h=P gives

$$T_h = T_0 + \frac{(K_L + K_B)P}{(2K_B + K_L)K_L}, \tag{8}$$

$$T_s = T_0 + \frac{(K_B)P}{(2K_B + K_L)K_L}. \tag{9}$$

After fitting a straight line to the plot of T_h and T_s versus P, we calculate K_B and K_L from the slopes. Since we know the geometry of the beam and the measured thermal conductance K_B, we determine

Author complimentary copy. Redistribution subject to AIP license or copyright, see http://jap.aip.org/jap/copyright.jsp

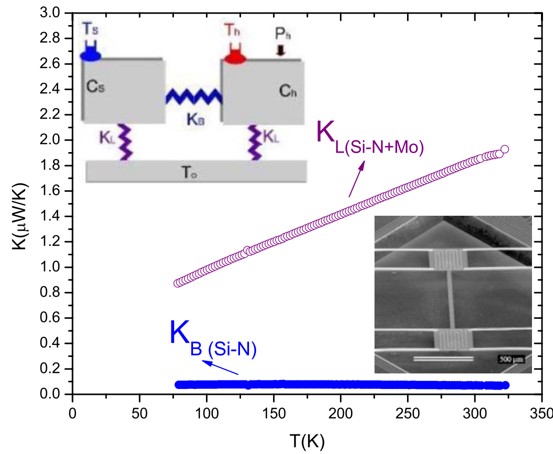

FIG. 6. (Color online) Thermal conductance through the legs (Si–N+Mo) and through the Si–N beam vs temperature. Upper left inset: Thermal model. Lower right inset: SEM micrograph of device.

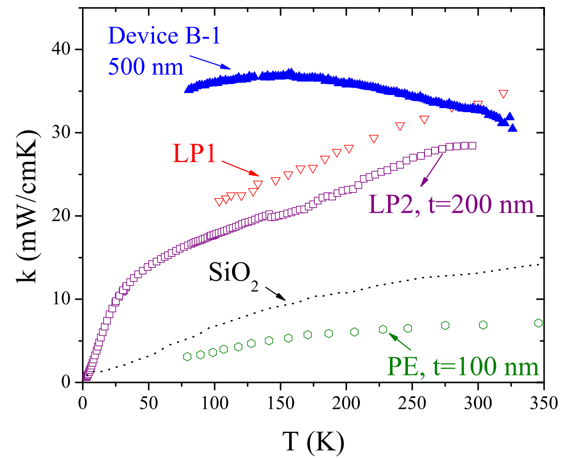

FIG. 7. (Color online) Comparison of our measured thermal conductivity of Si–N, $k_{(Si-N)}$, with previously reported values for LPCVD Si–N [LP1 (Ref. 13) and LP2 (Ref. 8)] and for PECVD (Ref. 10). Vitreous silica is shown for comparison [SiO_2 (Ref. 14)].

$$k_{\text{Si–N}} = \frac{K_B l}{wt}, \tag{10}$$

where l, w, and t are the length, width, and thickness of the beam, respectively.

B. Thermal conductivity of deposited thin films

In order to verify our experimental technique, we also present measurements of a device with a 200 nm thick Mo film sputtered on the Si–N beam (device C). The thermal conductance is measured using the same experimental technique described above. In this case, Mo adds a contribution to the beam, as shown in Fig. 2(c). A single subtraction of the background contribution due to the thermal conductance of Si–N ($K_{\text{Si–N}}$) gives the thermal conductance of our sample Mo thin film (K_S) and hence gives thermal conductivity of Mo (k_S).

$$K'_B = K_{\text{Si–N}} + K_S, \tag{11}$$

$$K_S = K'_B - K_{\text{Si–N}}, \tag{12}$$

$$k_S = \frac{K_S l}{wt}. \tag{13}$$

Here l, w, and t are the length, width, and thickness of the Mo film, respectively.

IV. RESULTS AND DISCUSSION

Figure 6 shows the thermal conductance through the Si–N beam, K_B, and through the legs, K_L, for device B. We see that K_B is much lower than K_L because the Mo wires deposited on the legs add a significant thermal conductance path. As we know the geometry of Si–N beam between the islands, we use Eq. (10) to convert thermal conductance K_B to thermal conductivity (k) of the Si–N beam. Figure 7 compares the resulting measured thermal conductivity of Si–N, $k_{\text{Si–N}}$, to previously reported amorphous Si–N films grown using LPCVD[8,9,13] and plasma enhanced chemical vapor deposition (PECVD),[10] as well as to vitreous silica (SiO_2).[14]

The high temperature values of our measured thermal conductivity of Si–N are in agreement with the earlier measurements of Si–N thin films. As the temperature drops, we see very little variation in our measured thermal conductivity of Si–N as a function of temperature. This is obviously a significant departure from the dependence seen in previously measured LPCVD Si–N films, and also deviates from the expected behavior in what we originally presumed was an amorphous film. The qualitative behavior of the measured and previously published data on Si–N is quite reminiscent of studies that compare thermal transport measured in both amorphous and polycrystalline allotropes of selenium and its alloys.[15,16] Note that the various LPCVD silicon nitrides shown in Fig. 6 have different thicknesses, and this could also play a role in the microstructure of the film and/or its thermal conductivity. The variation in k between the films grown with LPCVD and PECVD is also likely to be the result of different film microstructures.

The results of a preliminary investigation of the structure of several Si–N films all grown in the same LPCVD furnace under nominally identical conditions are shown in Fig. 8. Here x-ray diffraction data were collected using a Bruker D8 Discover diffractometer with Cu x-ray tube excited at 35 kV and 30 mA. Cu $K\alpha$ radiation was selected using an incident-beam graphite monochromator. The incident beam was collimated to the sample and data were collected using a two-dimensional (2D) multiwire proportional detector. 2D diffraction patterns were collapsed into the intensity versus diffraction angle 2θ one-dimensional traces for clarity by integrating over Debye rings (χ angle). The upper two plots, with apparent Bragg peaks at 13.8° and 20.3° indicate the likely presence of Si_3N_4 crystallites with a hexagonal crystal structure.[17] The position and particularly the width of the peaks are affected by the exact Si–N stoichiometry, crystallite size, and possible residual stress in the films. The variation in Si–N peak widths from sample-to-sample (and the absence of peaks in some films) suggests variations in crystallite size and possible inhomogeneity both across a wafer

Author complimentary copy. Redistribution subject to AIP license or copyright, see http://jap.aip.org/jap/copyright.jsp

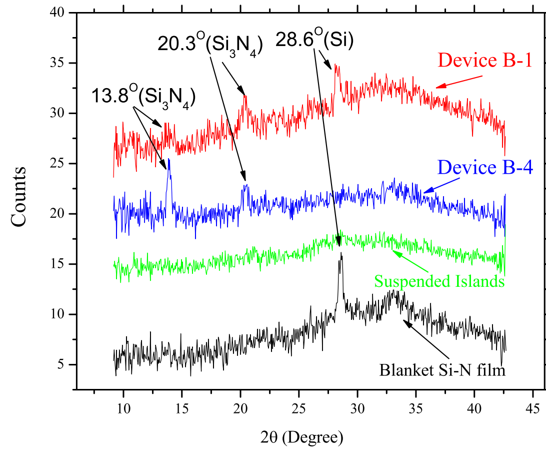

FIG. 8. (Color online) Results of preliminary structural investigation using x-ray diffraction (the upper three data sets are shifted vertically for clarity). Small but well-defined peaks are seen in scans for device B-1 and device B-4. Peaks caused by the underlying silicon are also visible, except when the substrate was slightly misaligned. Scans of suspended Si–N islands with no metal features and of an unpatterned Si–N film did not show observable crystallite peaks, but this is most likely due to the variation in crystallite size from run to run.

and from run to run. Further structural characterization is required to discern the micro- or nanocrystalline nature of the Si–N.

The possibility of inhomogeneous crystallization of the Si–N film could present challenges for our thermal conductivity measurements, where we plan to use a reference bridge fabricated on the same 1×1 cm^2 chip to measure the background contribution. The use of polycrystalline Si–N in the beams offers no impediment to this measurement scheme as long as large nonuniformities do not occur on these rather short length scales across the wafer. As shown in Fig. 9, the thermal conductivity data on several beams taken from different locations on a single wafer are closely grouped, with the worst deviation only as large as $\sim$10%, suggesting that despite the possibility of inhomogeneity in the nano- or microstructures of the Si–N, the background contribution of the beam is predictable, but should be periodically verified. The largest variation observed to date, for device B-3, is most likely due to micro- or nanostructural inhomogenity in the Si–N, but could also be related to moderate heating (several hours at temperatures between 150 and 200 °C) during a previous experiment with this particular device, although heating to these rather low temperatures (less than one-fourth the growth temperature, and an even smaller fraction of the expected melting temperature) would not normally significantly alter the structure of a film. However, since the thermodynamics of the silicon-nitride clearly requires further study, a partial low-temperature annealing cannot be excluded.

Figure 10 compares the thermal conductance of the Si–N beam with and without the 200 nm thick Mo sample film. At these temperatures, addition of the metal film simply adds to the total thermal conductance of the beam, resulting in the top curve in Fig. 10. Subtracting the previously measured thermal conductance of the beam ($K_{\text{Si–N}}$) isolates the contribution of the Mo film, which in this case is large compared

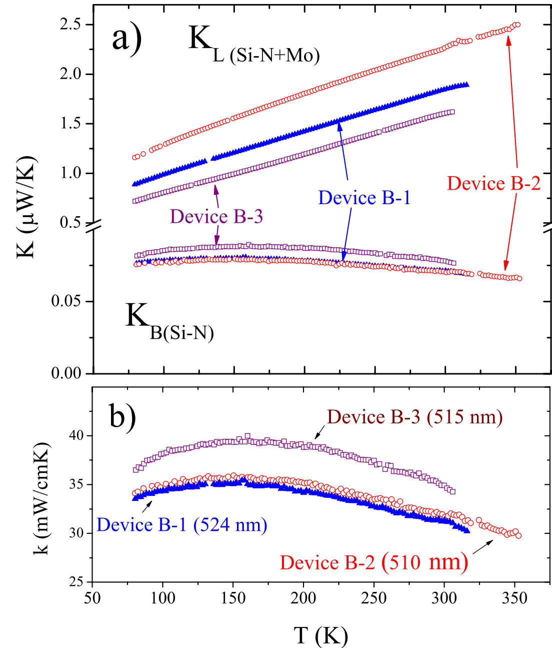

FIG. 9. (Color online) Comparison of results from three thermal platforms (of the device B type) fabricated on a single Si wafer. (a) Measured thermal conductances, K_L, shown above the axis break and, K_B, shown below. The large differences in K_L are caused by thickness variation in the Mo leads that dominate the leg thermal conductance. (b) Thermal conductivity of the Si–N forming the three bridges. Thicknesses were measured at several points on the frame of each platform by ellipsometry; the resulting error is approximately ±3 nm on each measurement. Devices B-1 and B-2 give very similar thermal conductivity, while device B-3 is somewhat higher, but still within $\sim$10% of the other values.

to the background of the beam. The known geometry of the film allows determination of the measured thermal conductivity of the Mo. The resulting thermal conductivity is shown in Fig. 11, which also demonstrates the accuracy of our experimental technique of measuring thermal conductivity of thin films. Since measurement of the temperature of each island involves measuring the resistance of each Mo thermometer as a function of temperature, resistivity and electrical conductivity of Mo as a function of temperature are easily determined using the known geometry of the resistors.

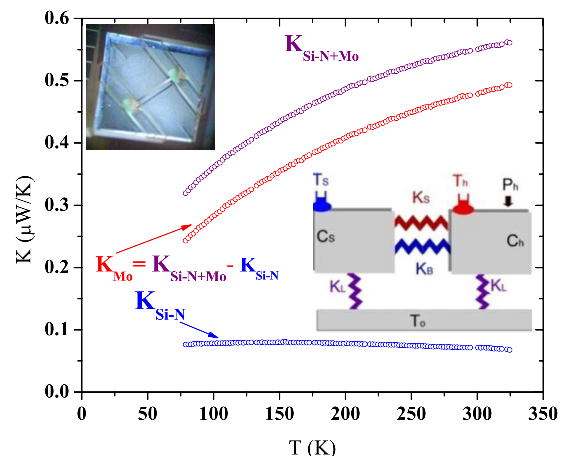

FIG. 10. (Color online) Comparison of thermal conductance K_B with $K_{S(\text{Mo})}$ after background subtraction $K_{S(\text{Mo})}=[(K_{\text{Si–N+Mo}})-(K_{\text{Si–N}})]$. Upper left inset: Optical picture of device. Lower right inset: Thermal model.

Author complimentary copy. Redistribution subject to AIP license or copyright, see http://jap.aip.org/jap/copyright.jsp

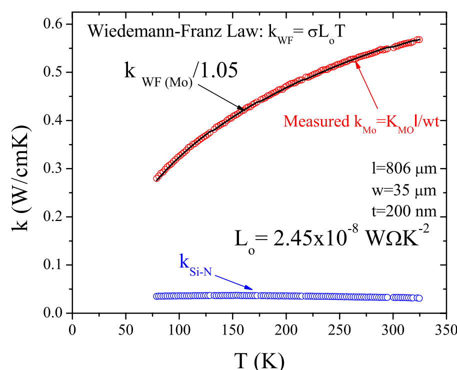

FIG. 11. (Color online) Thermal conductivity of measured $k_{S(\mathrm{Mo})}$ compared with measured $k_{\mathrm{Si-N}}$ and Wiedemann–Franz $k_{\mathrm{WF(Mo)}}$ (divided by a scale factor of 1.05).

Figure 11 compares our measured thermal conductivity of Mo, $k_{S(\mathrm{Mo})}$, determined from Eqs. (11)–(13), with the Weidemann–Franz thermal conductivity of $k_{\mathrm{WF(Mo)}}$. The measured data match extremely well with the Wiedemann–Franz thermal conductivity after introducing a scaling factor of 1.05. This slight difference between $k_{S(\mathrm{Mo})}$ and $k_{\mathrm{WF(Mo)}}$ is most likely caused either by a small deviation in the sample geometry due to a thickness variation or by a slightly different Lorenz number.

V. CONCLUSION

We presented thermal conductivity measurements of micromachined low-stress Si–N beams and Mo thin film from 77–325 K. Near 300 K our results match earlier measurements of thermal conductivity of Si–N, and at lower temperatures show behavior similar to polycrystalline materials. x-ray diffraction indicates the presence of Si_3N_4 crystallites, suggesting that this material, which was presumed to be amorphous due to similar growth conditions as used for previously reported Si–N, has a more ordered structure that leads to significantly different thermal transport. Despite the deviation from the amorphous material, the Si–N beams have very similar thermal conductivities across a wafer. The measured thermal conductivity of a 200 nm thick Mo thin film agrees well with the prediction of the Wiedemann–Franz law. We are in the process of fabricating thermal platforms with different thicknesses of Si–N to check a possible thickness dependence, beginning a more detailed investigation of the structure of the Si–N, and also working to understand the physics of the Si–N beams at low temperatures by fabricating platforms with semiconducting thermometers.

ACKNOWLEDGMENTS

We would like to thank J. A. Beall, G. C. Hilton, and K. D. Irwin for many helpful discussions and other contributions, D. Balzar for the XRD scans and assistance in interpretation, D. Queen for general discussions of silicon-nitride, and A. Johnson and N. McNew for help with computing and laboratory infrastructure. We also acknowledge NIST, the ACS Petroleum Research Fund (Contract No. PRF 46498-G10), and the University of Denver PROF program for providing funds to support this work.

[1]A. Mavrokefalos, M. T. Pettes, F. Zhou, and L. Shi, Rev. Sci. Instrum. **78**, 034901 (2007).
[2]P. Kim, L. Shi, A. Majumdar, and P. L. McEuen, Phys. Rev. Lett. **87**, 215502 (2001).
[3]T. S. Tighe, J. M. Worlock, and M. L. Roukes, Appl. Phys. Lett. **70**, 2687 (1997).
[4]D. G. Cahill, Rev. Sci. Instrum. **61**, 802 (1990).
[5]C. A. Paddock and G. L. Eesley, J. Appl. Phys. **60**, 285 (1986).
[6]D. G. Cahill, W. K. Ford, K. E. Goodson, G. D. Mahan, A. Majumdar, H. J. Maris, R. Merlin, and S. R. Phillpot, J. Appl. Phys. **93**, 793 (2003).
[7]*Cryogenic Particle Detection*, Topics in Applied Physics Vol. 99, edited by C. Enss (Springer-Verlag, Berlin, 2005).
[8]B. L. Zink and F. Hellman, Solid State Commun. **129**, 199 (2004).
[9]W. Holmes, J. M. Gildemeister, P. L. Richards, and V. Kotsubo, Appl. Phys. Lett. **72**, 2250 (1998).
[10]S. M. Lee and D. G. Cahill, J. Appl. Phys. **81**, 2590 (1997).
[11]B. L. Zink, B. Revaz, J. J. Cherry, and F. Hellman, Rev. Sci. Instrum. **76**, 024901 (2005).
[12]D. W. Denlinger, E. N. Abarra, K. Allen, P. W. Rooney, M. T. Messer, S. K. Watson, and F. Hellman, Rev. Sci. Instrum. **65**, 946 (1994).
[13]S. Huxtable (unpublished).
[14]S. K. Watson and R. O. Pohl, Phys. Rev. B **68**, 104203 (2003).
[15]F. J. Bermejo, E. Enciso, A. Criado, J. L. Martínez, and M. Garcia-Hernández, Phys. Rev. B **49**, 8689 (1994).
[16]R. Wawryk, C. Marucha, K. Balcerek, B. M. Terzijska, and Z. G. Ivanova, Cryogenics **40**, 749 (2000).
[17]ICDD Powder Diffraction File Card Nos. 41-0360 and 33-1160.

Author complimentary copy. Redistribution subject to AIP license or copyright, see http://jap.aip.org/jap/copyright.jsp